Research Square

Preprints are preliminary reports that have not undergone peer review.
They should not be considered conclusive, used to inform clinical practice,
or referenced by the media as validated information.

Capturing Metastable Electrocatalytic Active Structures with Atomic Resolution

David Muller

dm24@cornell.edu

School of Applied and Engineering Physics, Cornell University https://orcid.org/0000-0003-4129-0473

Zixiao Shi

Cornell University https://orcid.org/0000-0002-4414-655X

Qihao Li

Cornell University https://orcid.org/0000-0002-1124-1999

Andrés Molina Villarino

Cornell University https://orcid.org/0000-0003-3272-5156

Michael Colletta

Cornell University https://orcid.org/0000-0002-2571-8954

Noah Schnitzer

Cornell University https://orcid.org/0000-0002-1042-1146

Mihail Krumov

Cornell Univerisity

Christopher Pollock

Cornell University https://orcid.org/0000-0001-5736-513X

Guanxing Li

King Abdullah University of Science and Technology

Yimo Han

Rice University https://orcid.org/0000-0003-0563-4611

Héctor Abruña

Cornell University https://orcid.org/0000-0002-3948-356X

Physical Sciences - Article

Keywords:

Posted Date: April 23rd, 2026

DOI: https://doi.org/10.21203/rs.3.rs-9175550/v1

License: This work is licensed under a Creative Commons Attribution 4.0 International License.
Read Full License

Additional Declarations: There is **NO** Competing Interest.

Capturing Metastable Electrocatalytic Active Structures with Atomic Resolution

Zixiao Shi[1*]†, Qihao Li[1]†, Andrés Molina Villarino[1], Michael Colletta[2], Noah Schnitzer[3,4], Dasol Yoon[3], Mihail R. Krumov[1], Christopher J. Pollock[5], Guanxing Li[2,4], Yimo Han[6*], Héctor D. Abruña[1*], David A. Muller[2,4*]

[1] *Department of Chemistry and Chemical Biology, Cornell University, Ithaca, New York 14853, USA*

[2] *School of Applied and Engineering Physics, Cornell University, Ithaca, NY 14853, USA.*

[3] *Department of Materials Science and Engineering, Cornell University, Ithaca, New York 14853, USA*

[4] *Kavli Institute at Cornell for Nanoscale Science, Ithaca, NY 14853, USA.*

[5] *Cornell High Energy Synchrotron Source, Wilson Laboratory, Cornell University, Ithaca, NY 14853, USA,*

[6] *Department of Materials Science and Nanoengineering, Rice University, Houston, TX 77006, USA*

†These authors contributed equally to this work

Abstract

Pinpointing the active sites where electrocatalytic reactions occur requires atomic resolution and is fundamental to rational catalyst design [1–3]. In water electrolysis, the oxygen evolution reaction (OER) is driven by highly oxidizing potentials that typically transform electrocatalysts into metastable structures with high oxidation states, often reaching +4, even to +6 [4–12]. However, these metastable structures relax back once the potential is removed, complicating the identification of the true active structure and undermining long-term catalyst stability [13]. Using atomic-resolution cryogenic scanning transmission electron microscopy (Cryo-STEM), we directly visualized the metastable structure of a widely used OER electrocatalyst, nickel–iron (oxy)hydroxides, under operating conditions. Combining in-situ X-ray absorption spectroscopy, Cryo-STEM and electrochemical measurements, we find low(er) oxidation states (Fe^{3+} and Ni^{2+}) are preserved during catalysis and are sufficient to drive the reaction efficiently, contrary to conventional expectations that high-oxidation-state sites are essential for strongly oxidizing reactions.[7,12] Meanwhile, this electrocatalyst exhibits 2.2 A/cm^2 at 1.8 V, in anion exchange membrane water catalysts, a state-of-the-art performance. These findings experimentally demonstrate an apparent thermodynamic anomaly: that low(er)-oxidation-state sites can efficiently drive highly oxidizing reactions, paving the way to design durable OER electrocatalysts.

Main

In most catalysts, only a small portion of atoms, called active sites, actually drive the reaction. Identifying these active sites is essential for understanding how catalysts work and how to improve them [1–3]. In electrocatalysis, this challenge is magnified by the need for atomic-resolution characterization at the surface monolayers under operating conditions [14]. Under applied potential, these surface atoms experience extreme oxidizing or reducing conditions, often transforming into metastable structures with altered oxidation states [3,15,16]. When the potential is released, they may revert toward their original state, introducing structural disorder that might weaken its activity.

Oxygen evolution reaction (OER) catalysts exemplify this challenge: the high applied potentials needed to split water also oxidize the surface of metal or alloy electrocatalysts into oxyhydroxides [1,13,17–20]. Among OER catalysts, nickel-iron oxyhydroxides (NiFeOOH) stand out for their abundance and high catalytic activity, making them widely studied and industrially applied [21–24]. Yet they are unstable once the potential is turned off, reverting to nickel-iron hydroxides ($NiFe(OH)_2$), which hinders *ex-situ* characterization and compromises long-term catalyst durability [21]. *In-situ* and *operando* methods have been developed to track structural and oxidation-state changes in OER catalysts during operation [13,25–30], leading to a natural and common assumption that highly oxidized metal sites (+3 to +6) are essential for OER activity [4–12].

Here, we show that low(er)-oxidation-states electrocatalysts can also efficiently drive OER. Using atomic resolution cryogenic scanning transmission electron microscopy (Cryo-STEM, Fig. 1A, Extended Data Fig. 1), we directly imaged the metastable active structures of these OER electrocatalysts for the first time. By comparing the metastable structures of $Ni(OH)_2$ and $Ni(OH)_2$@FeOOH (Fig. 1B) with monolayer-level structural difference under OER conditions using a combination of *in-situ* X-ray absorption spectroscopy (XAS) and Cryo-STEM, we identify the active sites responsible for catalytic activity. Remarkably, while oxidized regions are poorly active, the regions that maintain low(er) oxidation states (Fe^{3+} and Ni^{2+}) under strong oxidizing conditions still drive OER efficiently, an apparent thermodynamic paradox, that can be rationalized by kinetic effects.

More broadly, our approach provides a generalizable experimental framework for capturing metastable active structures in electrochemical reactions, offering new guidance for designing both highly active and durable electrocatalysts.

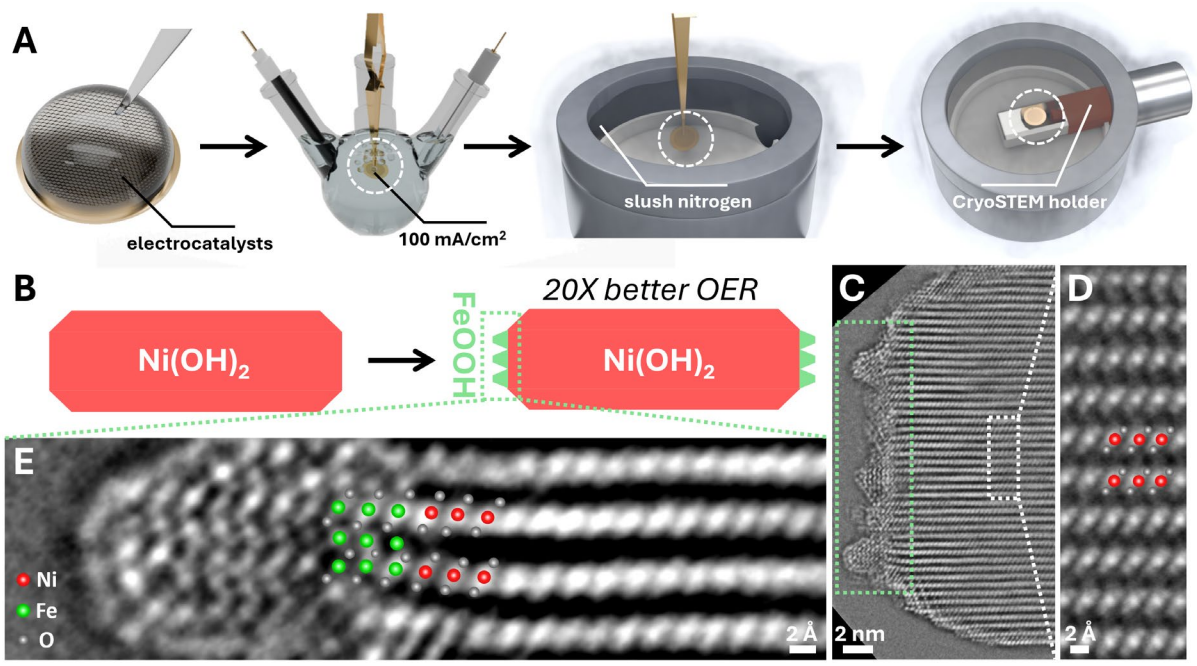


Fig. 1 Cryo-STEM and catalyst platforms for identifying metastable active catalyst structures (A) Schematic of the Cryo-STEM workflow: electrocatalysts are operated under OER conditions with (100 mA cm^{-2} for 100 mins) on HexAuFoil grids, then rapidly quenched in slush nitrogen and transferred for imaging to capture metastable active structures. (B) Structural comparison of $Ni(OH)_2$ and $Ni(OH)_2$@FeOOH, where the addition of only a few FeOOH monolayers on edge plane lead to ~20 fold enhancement in OER activity. (C) atomic resolution STEM-iDPC image of $Ni(OH)_2$@FeOOH from the [100] side view, the green box highlights the FeOOH grown selectively on $Ni(OH)_2$ edge planes. (D) Zoomed-in region shows the interior β-$Ni(OH)_2$ core, highlighting its layered structure, and (E) the epitaxial growth of δ-FeOOH nanoisland on the β-$Ni(OH)_2$ edge plane surface. These combined STEM-EELS and iDPC results confirm the lateral heterostructure of the $Ni(OH)_2$@FeOOH, emphasizing the selective, epitaxial growth of δ-FeOOH on the {100} edge planes of β-$Ni(OH)_2$.

Monolayer-Level Structural Changes Drive Performance Gains

Identifying the active structure in electrocatalysts is challenging not just because of their dynamic nature under operating conditions, but also due to the structural complexity of the catalysts themselves. To isolate the structural features responsible for catalytic activity, we designed electrocatalysts with subtle, well-resolved differences that lead to large differences in performance. This approach minimizes confounding variables and enables a direct, atomic-level correlation between structure and activity (Fig. 1B).

To attribute catalytic activity to specific structural features, it is essential to control which crystal facets are exposed, as different facets often exhibit distinct reactivity. Ni(Fe) (oxy)hydroxides are layered two-dimensional (2D) materials, composed of stacked sheets held together by van der Waals forces along the c-axis [4,27,31,32]. This reduced dimensionality simplifies the system and allows the surface to be categorized into basal planes {001}, edge planes {100}, and truncated planes{10X}, as exemplified In our synthesized $Ni(OH)_2$ (Fig. S1).

Building on this rationale, we synthesized three highly crystalline and faceted Ni(Fe) (oxy)hydroxide nanoplates ($Ni(OH)_2$, $Ni(OH)_2$@FeOOH, and $NiFe(OH)_2$, full formula in SI) with uniform shape and sizes Their geometric and chemical uniformity ensures representative imaging, while their high crystallinity facilitates atomic-resolution structural analysis (Fig. S2-S13). It is worth mentioning that, although NiFe hydroxides have been widely studied, their atomic-resolution imaging along cross-section have been rarely reported.

Pure $Ni(OH)_2$ or pure FeOOH are known to exhibit poor OER activity, compared to the $NiFe(OH)_2$, where Fe is homogenously incorporated into the $Ni(OH)_2$ lattice and shows significantly improved performance [33,34]. In contrast to this conventional structure [4,6,31,33], our $Ni(OH)_2$@FeOOH features δ-FeOOH as a separate crystalline phase that grows selectively and epitaxially on the edge planes of $Ni(OH)_2$, while the truncated and basal planes remain Fe-free, forming in a lateral heterostructure (Fig. 1B, S2-S4). This anisotropic distribution of Fe is confirmed by atomic-resolution STEM integrated differential phase contrast (iDPC) imaging and electron energy loss spectroscopy (EELS), which together reveal the δ-FeOOH and β-$Ni(OH)_2$ crystalline phases and their spatial distribution (Fig. 1C-E, S6-S8, Extended Data Fig. 2-3) [35]. The resulting structural contrast -- just a few monolayers of FeOOH on the $Ni(OH)_2$ edge planes -- makes $Ni(OH)_2$@FeOOH an ideal platform for pinpointing the atomic-scale origin of high OER activity.

In terms of OER performance, cyclic voltammetry (CV, Fig. 2A) shows that pure $Ni(OH)_2$ is a poor OER electrocatalyst ($\eta > 500$ mV at 10 mA/cm²), as expected [33]. $Ni(OH)_2$@FeOOH, in contrast, despite containing only ~2 wt% Fe, achieves significantly better performance ($\eta = 320$ mV at 10 mA/cm²), surpassing that of $NiFe(OH)_2$ ($\eta = 340$ mV at 10 mA/cm²), which contains ~20 wt% Fe homogeneously incorporated into the lattice (Fig. 2A). In conventional $NiFe(OH)_2$, OER activity typically scales with Fe content up to ~30% [4,6,36], yet the lateral heterostructure of $Ni(OH)_2$@FeOOH achieves higher activity with far less Fe. This result highlights that, in addition to Fe concentration, its spatial arrangement -- particularly confinement to the $Ni(OH)_2$ edge plane as FeOOH -- is also important.

While our primary goal is to identify the active structure rather than optimize full-cell engineering, our $Ni(OH)_2$@FeOOH already supports high current densities in an anion exchange membrane water electrolyzer (AEMWE), reaching 2.2 A/cm^2 at 1.8 V and 7.2 A/cm^2 at 2.2 V (Fig. S14). This performance compares favorably with NiFe based, and even precious-metal-based water electrolyzers in the literature [37–40], suggesting substantial headroom for further improvements through electrode and cell optimization .

The enhanced activity of $Ni(OH)_2$@FeOOH is consistent with prior proposals that Fe-sites on the edge planes of NiFe (oxy)hydroxides contribute disproportionately to OER activity [41,42]; in our case, this motif is selectively concentrated at the edge planes, maximizing its exposure. However, the specific atomic-scale structure responsible for this reactivity is revealed in the next section using in-situ XAS and Cryo-STEM. Because all three nanoplates have comparable sizes and facet exposure, the performance differences can be directly correlated with their local structural variations, setting the stage for identifying active structures at the atomic scale.

Low(er)-Oxidation-State OER Electrocatalyst

We further investigate their active structure and corresponding oxidation state change during OER. As stated in the introduction, OER operates at such a high potential (>1.6 eV vs. RHE) that, even Au is oxidized (Au → Au^{3+} + $3e^-$ at 1.53 V vs. RHE). It is thus surprising that, despite its high catalytic activity, $Ni(OH)_2$@FeOOH maintains a rather low oxidation state under OER conditions: contradicting the widely held assumption that high-valence $Ni^{3+/4+}$ or $Fe^{3+/4+}$ species are essential for activity. Cyclic voltammetry (CV) and in-situ X-ray absorption spectroscopy (XAS) under OER conditions provide this information.

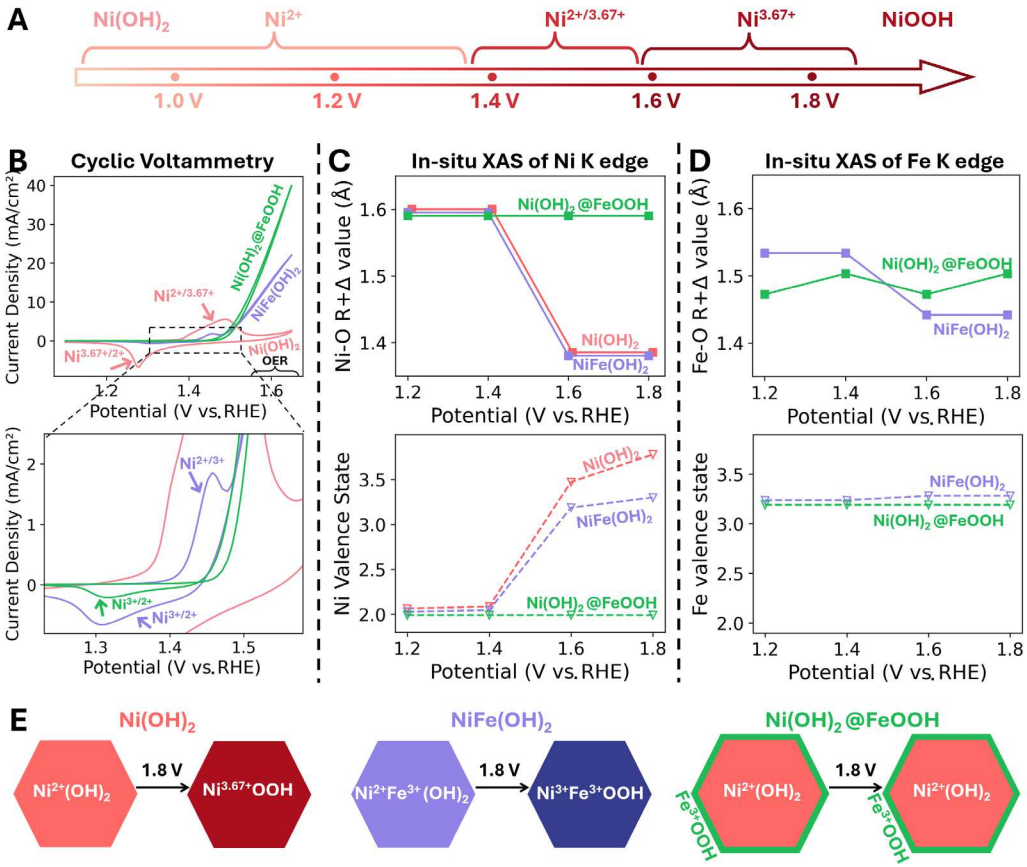


Fig. 2 Ni in $Ni(OH)_2$@FeOOH remains predominantly Ni^{2+} under OER conditions

(A) Ni oxidation state changes in $Ni(OH)_2$ during OER, derived from experimental data. (B) Cyclic voltammetry (CV) curves of $Ni(OH)_2$ (pink), $NiFe(OH)_2$ (purple, 20% Fe incorporated), and $Ni(OH)_2$@FeOOH (green, 2% Fe selectively on edge planes) in 1 M Fe-free KOH solution. $Ni(OH)_2$ exhibits a distinct $Ni^{2+/3.67+}$ oxidation peak, and $NiFe(OH)_2$ shows a clear $Ni^{2+/3+}$ oxidation peak. In contrast, $Ni(OH)_2$@FeOOH displays only a minor $Ni^{3+/2+}$ reduction peak, indicating Ni predominantly remains in the Ni^{2+} state under OER conditions. No iR-drop correction is applied in all electrochemical data. (C–D) Electrochemical *in-situ* Ni and Fe edge XAS measurements of the electrocatalysts under OER provide complementary insights into the Ni-O/Fe-O bond lengths and the Ni/Fe valence states at various potentials. In $Ni(OH)_2$ and $NiFe(OH)_2$, Ni undergoes Ni^{2+} to $Ni^{3+/4+}$ oxidation coupled with Ni-O shell peak value decreasing. Similarly, Fe in $NiFe(OH)_2$ shows Fe-O shell peak contraction, reflecting its lattice integration and coupling with Ni oxidation. In contrast, Ni and Fe valence states in $Ni(OH)_2$@FeOOH remain nearly unchanged, confirming the suppression of Ni oxidation. (E) Schematic illustration summarizing Ni oxidation behavior: Ni in $Ni(OH)_2$ and $NiFe(OH)_2$ oxidizes to $Ni^{3+/4+}$, while Ni in $Ni(OH)_2$@FeOOH predominantly remains Ni^{2+} under OER conditions.

CV curves reveal the Ni oxidation state behavior. In $Ni(OH)_2$, Ni undergoes oxidation from Ni^{2+} to $Ni^{3.67+}$ (calculated from oxidation peak charge integration, see SI for details) where 3.67+ of Ni is well-established feature of pure NiOOH [4,6,18,33,43] (Fig. 2B, full formula in SI). Unlike precious metal electrocatalysts like Pt, where the redox peak primarily arises from surface reactions, the entire hydroxide nanoplate, including both surface and bulk, undergo redox reactions and contribute to the redox signature in these Ni and NiFe (oxy)hydroxide systems.

In contrast to $Ni(OH)_2$ and $NiFe(OH)_2$, $Ni(OH)_2$@FeOOH, with FeOOH covering the $Ni(OH)_2$ edge planes, shows a markedly suppressed Ni redox peak (Fig 2B), indicating that the Ni redox reaction is largely hindered. This contrast highlights a surprising picture: in $Ni(OH)_2$@FeOOH, Ni remains predominantly in the low-valence Ni^{2+} state under highly oxidizing conditions, yet the catalyst exhibits high catalytic activity.

To further probe this apparent thermodynamic anomaly, we performed electrochemical *in-situ* XAS under OER conditions, which provides structural information regarding average bond lengths and valence state of Ni and Fe sites under OER conditions. Ni center oxidation states extracted from XAS edge energies (see SI for details) indicates that, in $Ni(OH)_2$ and $NiFe(OH)_2$, Ni^{2+} undergoes oxidation to $Ni^{3.8+}$ and $Ni^{3.4+}$ respectively in NiOOH and NiFeOOH, under OER potentials (1.8 V vs. RHE), accompanied by a Ni–O shell peak (R+Δ) shortening from 1.60 Å to 1.39 Å (Fig. 2C, Extended Data Fig. 4, Fig. S16, full formula in SI), in agreement with previous studies [4,5,23,44,45]. However, in $Ni(OH)_2$@FeOOH, Ni remains largely Ni^{2+} even at 1.8 V vs. RHE, and with an unchanged Ni–O shell peak (~1.60 Å (R+Δ)), consistent with the small redox peak in the CV (Fig. 2B), indicating no obvious valence state change of Ni during OER (Fig. 2C, Extended Data Fig. 5).

Similarly, for Fe in $NiFe(OH)_2$, the Fe–O shell peak (R+Δ) shortens from 1.53 Å to 1.44 Å in NiFeOOH under OER conditions, coupling to its Ni site structural change during OER. In contrast, Fe in $Ni(OH)_2$@FeOOH, existing as 1–2 nm δ-FeOOH nanoislands on the edge planes, remains almost structurally and chemically intact, showing no obvious changes even at 1.8 V vs. RHE during OER (Fig. 2D).

Together, the CV and in-situ XAS results point to a surprising phenomenon: our $Ni(OH)_2$@FeOOH electrocatalyst maintains predominantly low-valence Ni^{2+} under OER conditions while exhibiting high catalytic activity (Fig. 2E). This finding contradicts the widespread view that Ni^{2+} is inherently oxidized to $Ni^{3+/4+}$ under OER potentials [4–6,28,31,33,42,46,47]. The presence of a small redox feature in the CV of $Ni(OH)_2$@FeOOH suggests that a minor fraction of Ni may still undergo oxidation, but the geometric distribution and chemical environment of these Ni^{3+} sites remain unknown at this stage. This puzzle will be solved in the next sections.

Cryo-STEM Captures Metastable Active Structure NiOOH

To address the puzzling stability of Ni^{2+} and active sites in $Ni(OH)_2$@FeOOH under OER conditions, we turned to Cryo-STEM, a technique both established and evolving [48–51]. The concept is to freeze the electrocatalysts rapidly right after the desired reaction takes place and to resolve their metastable structure(s), in which the active sites are embedded (Fig. 1A, Extended Data Fig. 1, Fig. S20).

Here, we first validated the ability of Cryo-STEM to resolve metastable structures at atomic resolution by applying it to $Ni(OH)_2$, which is known to oxidize into NiOOH under OER conditions. In pristine $Ni(OH)_2$ samples (before OER), STEM-HAADF imaging revealed the known β-$Ni(OH)_2$ crystalline structure (Fig. 3A). Notably, both basal and edge surfaces are covered with 1nm NiO (Fig. 3A, Fig. S4-5), indicating that a few monolayers on the $Ni(OH)_2$ surface can dehydrate under ambient conditions ($Ni(OH)_2 \rightarrow NiO + H_2O$) after synthesis.

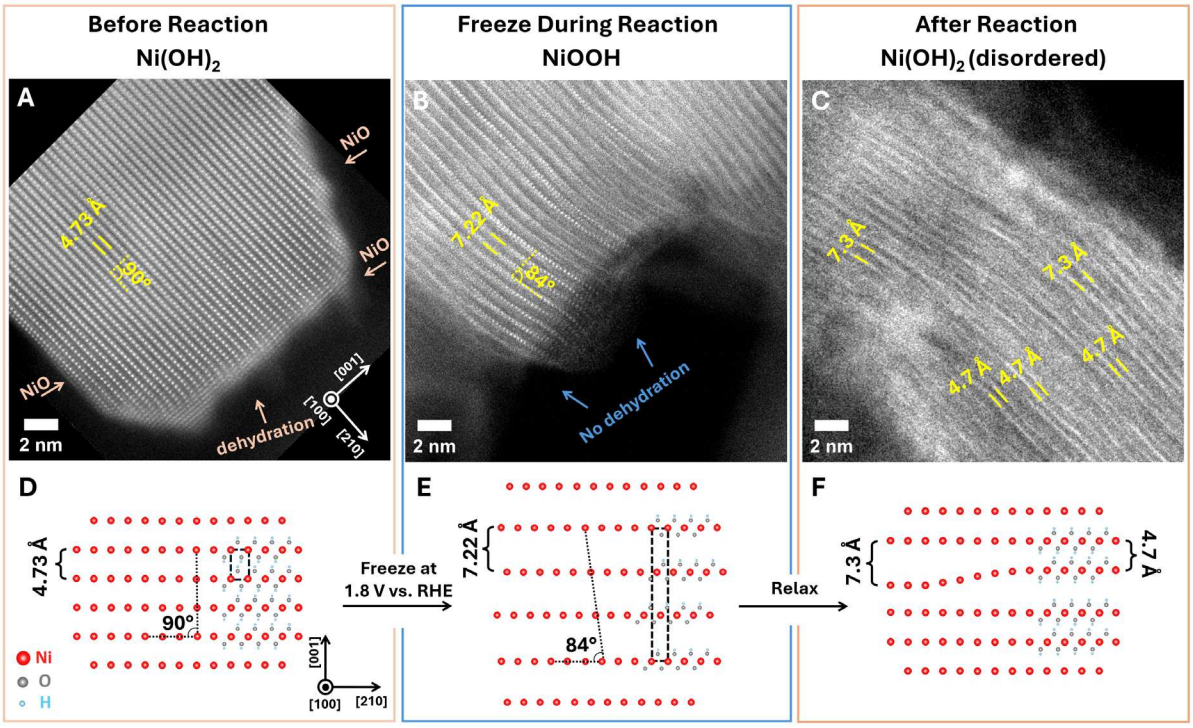


Fig. 3 Atomically resolved metastable active structure of $Ni(OH)_2$ during OER

(A) atomic resolution STEM-HAADF image of pristine $Ni(OH)_2$ before electrochemical testing. Fast Fourier transform (FFT) analysis confirms a 4.73 Å interlayer spacing for the (001) plane and a 2.78 Å in-plane Ni–Ni spacing along the (100) direction. Blue arrows indicate a dehydrated NiO surface layer on both basal and edge planes. (B) atomic resolution Cryo-STEM HAADF image of the active NiOOH phase, formed from $Ni(OH)_2$ under OER conditions and rapidly frozen in slush liquid nitrogen to preserve its structure. The image reveals a 7.22 Å interlayer spacing for the (003) plane and a shorter 2.53 Å in-plane Ni–Ni spacing along (100). Blue arrows show a fully preserved surface without dehydration, highlighting the ability of Cryo-STEM to image the surface of metastable structure NiOOH during OER. (C) HAADF image of disordered $Ni(OH)_2$, obtained by conventional *ex-situ* measurement after electrochemical testing. The structure shows a disordered phase with mixed interlayer spacings (4.6 Å and 7.3 Å), indicating the instability of NiOOH outside of OER conditions. (D-F) Atomic schematic illustrating the structural transformation from $Ni(OH)_2$ to NiOOH during OER and disordered $Ni(OH)_2$ decayed from NiOOH after OER. These results demonstrate that Cryo-STEM can successfully capture and resolve the atomic structure of the metastable NiOOH structure oxidized from .$Ni(OH)_2$ during OER.

Capturing the metastable structure of NiOOH, oxidized from $Ni(OH)_2$ during OER, presented a greater challenge. Once the OER applied potential is removed from the electrocatalysts,

NiOOH gradually reverts back to its thermodynamic equilibrium $Ni(OH)_2$ phase under ambient conditions, as confirmed by XAS measurements (Extended Data Fig. 6). To preserve its structure, we polarized $Ni(OH)_2$ at 1.8 V vs. RHE for 100 minutes on a HexAuFoil grid [52] to ensure a full conversion into NiOOH, followed by rapid freezing in slush liquid nitrogen (Fig. 1A, Extended Data Fig. 1, Fig. S20).

Cryo-STEM successfully visualized the atomic structure of the NiOOH (Fig. 3B). Cryo-STEM HAADF images captured two distinct structural features that differentiate NiOOH from $Ni(OH)_2$ (Fig. 3A, B). First, NOOH exhibits a 7.22 Å interlayer spacing and a 2.53 Å in-plane Ni–Ni bond length, compared to 4.73 Å and 2.78 Å, respectively, for $Ni(OH)_2$ (these d-spacings are determined by FFT in Fig. S22). Second, NiOOH adopts an AB–BC–CA stacking sequence, distinct from the AB–AB–AB stacking of $Ni(OH)_2$, which results in an angular shift between in-plane and interlayer Ni–Ni bonds from 90° in $Ni(OH)_2$ to 84° in NiOOH.

Importantly, Cryo-STEM also preserves the surface structure of NiOOH, without any dehydrated layer, compared to pristine $Ni(OH)_2$ (Fig. 3B). Moreover, this transformation was not a localized event: Cryo scanning electron nanobeam diffraction (SEND, a STEM technique) confirms the large-area structural transformation of $Ni(OH)_2$ to NiOOH by Cryo-SEND (Extended Data Fig. 7) [53].

While Cryo-STEM successfully resolves the crystalline NiOOH phase, STEM imaging of $Ni(OH)_2$ after OER reveals a heavily disordered structure (Fig. S22). We refer to this as disordered $Ni(OH)_2$, which shows both 7.3 Å and 4.6 Å interlayer spacings but lacks sufficient crystallinity to resolve in-plane Ni–Ni distances at atomic resolution (Fig. 3C).

The clear structural differences among $Ni(OH)_2$, NiOOH, and disordered $Ni(OH)_2$ demonstrate Cryo-STEM's ability to capture metastable active structure of OER electrocatalysts at the atomic scale. In the next section, we apply this approach to explore the origin of Ni^{2+} retention and atomic-scale active structure of $Ni(OH)_2$@FeOOH during OER.

FeOOH on $Ni(OH)_2$ Edge Plane is Catalytically Active

Where are the Ni^{2+}, possible $Ni^{3+/4+}$, and Fe^{3+} sites in the active structure of $Ni(OH)_2$@FeOOH during OER? In this section, we address the structural origin of Ni oxidation-resilience and the enhanced OER performance of $Ni(OH)_2$@FeOOH with a combination of Cryo-STEM and *in-situ* XAS.

Cryo-STEM imaging captures the metastable structure of $Ni(OH)_2$@FeOOH with atomic resolution, revealing that the $Ni(OH)_2$ core laterally surrounded by FeOOH at the edge planes remains as Ni^{2+} and structurally stable during the OER. In contrast, the $Ni(OH)_2$ layer directly exposed to the electrolyte (i.e. no FeOOH coverage on the truncated or basal planes) oxidizes into NiOOH under OER conditions (Fig. 4A-B). Together, the oxidized structure of $Ni(OH)_2$@FeOOH forms a unique sandwich heterostructure NiOOH@$Ni(OH)_2$@NiOOH within the lateral heterostructure $Ni(OH)_2$@FeOOH (Fig. 4A-B). Cryo-SEND further confirms the anisotropic structural transformation across a large field of view (Extended Data Fig. 8, Fig. S27). This structural change explains that the minor Ni redox peaks observed electrochemically originate from the oxidation of these $Ni(OH)_2$ layers without FeOOH covering on edge planes.

Oxidation of $Ni(OH)_2$ to NiOOH requires proton-coupled electron transfer (PCET, $Ni(OH)_2 + OH^- \rightarrow NiOOH + H_2O + e^-$ in base) [54]. The oxidation-resilience of $Ni(OH)_2$ in $Ni(OH)_2$@FeOOH suggests that this charge transfer is suppressed in both directions: out-of-plane (along the c-axis) due to NiOOH coverage on basal planes, and in-plane (a/b-axis) due to FeOOH surface coverage on edge planes. The charge transfer in $Ni(OH)_2$ may be intrinsically anisotropic, favoring in-plane over out-of-plane transfer, in which case NiOOH coverage may not be the dominant factor. Thus, by blocking in-plane charge transfer, edge-linked FeOOH prevents oxidation of the $Ni(OH)_2$ to NiOOH during OER.

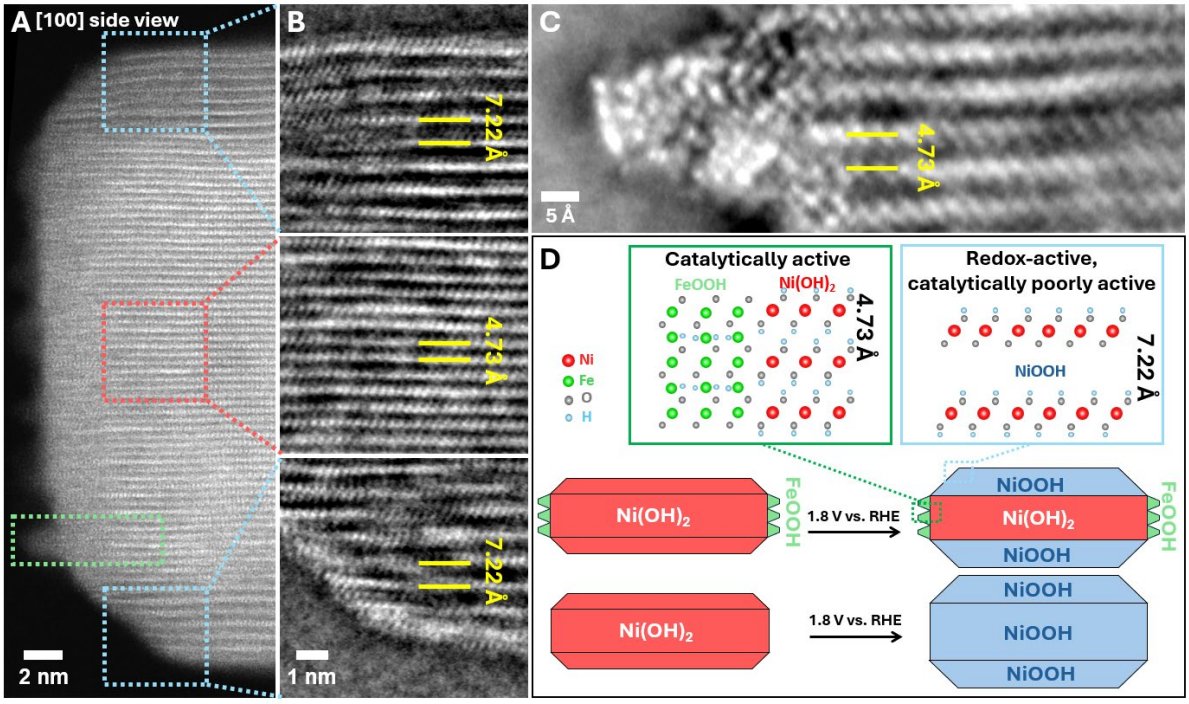


Fig. 4 Differentiate redox-active sites and catalytically active sites within $Ni(OH)_2$@FeOOH (A) atomic resolution Cryo-STEM HAADF image showing that the top and bottom $Ni(OH)_2$ layers, which lack δ-FeOOH coverage on their truncated planes, are oxidized to NiOOH, as indicated by the increased interlayer spacing of 7.22 Å. (B) The zoomed-in region of these top (blue), middle (red) and bottom (blue) $Ni(OH)_2$ layer presents a corresponding Cryo-STEM iDPC image, confirming that $Ni(OH)_2$ layers without δ-FeOOH coverage undergo oxidation (interlayer spacing increases from 4.73 Å to 7.22 Å), while those protected by δ-FeOOH on the {100} edge planes retain the $Ni(OH)_2$ structure with Ni^{2+}. (C) The zoomed-in region of surface δ-FeOOH linked to $Ni(OH)_2$ edge plane (green box in (A)) showing the FeOOH and $Ni(OH)_2$ structure remain its crystal structure (D) Schematic illustration based on Cryo-STEM results showing the metastable structure of $Ni(OH)_2$ and $Ni(OH)_2$@FeOOH under OER conditions. The δ-FeOOH on edge planes of $Ni(OH)_2$ block charge transfer within $Ni(OH)_2$, preventing oxidation. These findings suggest that δ-FeOOH covered on the $Ni(OH)_2$ edge planes is responsible for OER activity while the Ni^{2+} in the $Ni(OH)_2$ core remains unoxidized in $Ni(OH)_2$@FeOOH .

The Fe in surface FeOOH remains Fe^{3+} during OER, confirmed by the combination of Cryo-STEM and *in-situ* XAS. The FeOOH epitaxially grown on the $Ni(OH)_2$ edge plane consists of only 2 – 4 monolayers, forming a mixture of nanoislands and flat layers, with at least 25% of Fe atoms exposed as surface. *In-situ* XAS shows no significant change in Fe oxidation state during

OER, indicating that these surface-exposed Fe atoms remain as Fe^{3+}. Cryo-STEM further reveals that the adjacent $Ni(OH)_2$ to FeOOH retains the structure of β-$Ni(OH)_2$ (Fig. 4C), confirming that the Ni sites linked to FeOOH remain as Ni^{2+}.

The active structure of $Ni(OH)_2$@FeOOH is then revealed as the δ-FeOOH epitaxially grown on the β-$Ni(OH)_2$ edge plane. This identification stems from the comparison between the metastable active structures of NiOOH and $Ni(OH)_2$@FeOOH (Fig. 3B, Fig. 4, Extended Data Fig. 9). The surface structures they have in common are the NiOOH truncated and basal planes, which experience oxidation but are catalytically poorly active. The surface structures they differ in are the NiOOH edge planes and the FeOOH monolayers on the $Ni(OH)_2$ edge planes, while the latter contributes to around 20 times better OER performance. Together, these observations distinguish between redox-active and active sites in $Ni(OH)_2$@FeOOH: while high-oxidation-state $N^{3+/4+}$ sites in NiOOH on all edge/truncated/basal planes are relatively catalytically inactive, the Fe^{3+} in FeOOH grown on the $Ni(OH)_2$ edge planes remains Fe^{3+} and Ni^{2+} and account for this enhanced OER performance.

Conclusion

In summary, we directly visualized the metastable active structures of OER catalysts at atomic resolution, revealing that low-oxidation-state sites can remain both stable and catalytically active under highly oxidizing conditions. In our monolayer-engineered $Ni(OH)_2$@FeOOH electrocatalyst, $Ni(OH)_2$ regions without FeOOH coverage oxidize to NiOOH ($Ni^{3.67+}$) yet exhibit poor activity, whereas FeOOH-covered $Ni(OH)_2$ edge planes maintain Ni^{2+} and Fe^{3+} states that efficiently drive OER. This finding contrasts with the common guideline that high-oxidation-state metal species are essential in OER catalysis. Instead, it reveals that oxidation-resilient sites -- those that remain relatively low oxidation states -- can sustain activity while preserving structural integrity. More broadly, our cryo-STEM approach establishes a general framework for capturing and identifying metastable active structures in electrocatalysts, offering new design principles for achieving both high activity and long-term durability in electrocatalysts.

Methods

Sample Synthesis

Synthesis of $Ni(OH)_2$ nanoplates

$Ni(OH)_2$ nanoplates were synthesized with the hydrothermal method modified by the reported recipe [55]. Briefly, 20 mmol $Ni(NO_3)_2 \cdot 6H_2O$ (99.999%, Aldrich) was dissolved in 40 mL DI water under stirring. 15 mL of 1 M KOH (99.99%, Aldrich) solution was slowly added dropwise, forming a cyan suspension that was stirred for an additional 30 min. The suspension was purified through centrifugation, sonication, and redispersion steps with DI water. The resulting suspension was transferred to a 50 mL PTFE-lined autoclave and heated at 160 °C for 2 h. After cooling, the precipitate was washed, centrifuged, and freeze-dried to yield a dense cyan powder.

Synthesis of $Ni(OH)_2$@FeOOH nanoplates

$Ni(OH)_2$@FeOOH nanoplates were synthesized by wet chemical deposition using $Ni(OH)_2$ nanoplates as templates. Briefly, 1 mmol $Ni(OH)_2$ powder was dispersed in 100 mL DI water via sonication. A 10 mL aliquot of a separately prepared $Fe(CH_3COO)_2$ (98%, Aldrich) solution (0.2 mmol in 100 mL DI water) was slowly added dropwise to the $Ni(OH)_2$ suspension under continuous stirring, and the solution was stirred overnight. The obtained product was purified by washing, centrifugation, and freeze-drying, yielding a dense, light green-blue powder.

Synthesis of $NiFe(OH)_2$ nanoplates

$NiFe(OH)_2$ nanoplates were synthesized with the hydrothermal method modified by the reported recipe [56]. 2 mmol $Ni(NO_3)_2 \cdot 6H_2O$ and 0.4 mmol $Fe(NO_3)_3 \cdot 9H_2O$ (98%, Aldrich) were dissolved in 20 mL DI water under stirring to form a light-green solution. Then, 4.8 mmol triethanolamine (TEA, 99%, Sigma) was added dropwise, producing a transparent orange solution. After 30 minutes of stirring, 4.2 mmol urea (99.0%, Sigma) was added. The solution was transferred to a 50 mL PTFE-lined autoclave and heated at 160 °C for 24 h. After natural cooling, a yellow precipitate was collected, washed with DI water via sonication and centrifugation, and freeze-dried to obtain $NiFe(OH)_2$ as a dense yellow powder.

Electrochemistry Characterization

Electrochemistry Characterization

Electrochemical characterization was conducted in a standard three-electrode system using a glassy carbon (GC) electrode with a 5.5 mm diameter as the working electrode (WE), a carbon rod as the counter electrode (CE), and a home-made reversible hydrogen electrode (RHE) as the reference electrode (RE). All experiments were carried out in 1 M KOH (Thermo Scientific Chemicals, 99.98%) with Fe impurity removed using a previously reported method [57]. The Fe-free nature of 1M KOH solution can be verified by the degrading OER activity of pure $Ni(OH)_2$. The potentials were reported with RHE as reference without any iR compensation.

The electrocatalysts were dispersed in 0.1 wt% Nafion solution (75% water, 25% ethanol) and sonicated in an ice bath to form a homogeneous ink with a concentration of 1 mg mL^{-1}, as low loading is recommended to fully oxidize the hydroxides electrocatalysts [58]. Subsequently, 10 μL of the desired electrocatalyst ink was drop-cast onto the GC electrode and dried at a rotation speed of 500 rpm, resulting in a loading of 42.0 μg cm^{-2}. OER polarization curves were obtained in Ar-saturated 1 M KOH with a rotation rate of 1600 rpm and scan rate of 5 mV/s using a WaveDriver 10 potentiostat system (Pine Instruments, USA). Ultra-high-purity Ar was bubbled through KOH during the measurement.

MEA Fabrication and WE tests (no longer than 150 words): Membrane electrode assemblies were made by a homemade ultrasonic spray station. Quaternary ammonium poly(N-methyl-piperidine-co-p-terphenyl) (QAPPT) alkaline polymer electrolyte was used as both membrane (25 μm) and ionomer (80 mg mL-1 in DMSO). The catalysts loadings were 0.4 mg PtRu cm^{-2} in the cathode (60%PtRu/C, Fuel Cell Store) and 2 mg cm^{-2} $Ni(OH)_2$@FeOOH in the anode, with an active area of 2×2 cm2. The electrolyzer was assembled in a custom-designed cell using PTFE gaskets (270 μm) and tightened to a torque of 4 N·m. The cell was tested at 80 °C using a CT3002N battery cycler (LANHE, China), the cell was activated by gradually increasing the voltage from 1.7 V to 2.2 V. After the current stabilized, data points were collected by decreasing the cell voltage from 2.2 V to 1.3 V in 0.05 V increments.

Calculation of charge transfer per Ni

The oxidation state of Ni can be estimated from the oxidation peak in the CV curve before the onset of the OER. The total charge transfer Q is calculated by:

$$Q = \frac{\int I \cdot dE \cdot A}{s}$$

Where I is the current density, E is the potential, A is the surface area of the glassy carbon electrode, and s is the scan rate.

The total electron charge, n_e, and the number of Ni sites in the electrocatalyst n_{Ni} can be calculated by

$$n_e = \frac{Q}{F}$$

$$n_{Ni} = \frac{m * \alpha}{M}$$

Where F is the Faraday constant, m is the mass of electrocatalyst, M is the molar mass of electrocatalyst, and α is the metal ratio of Ni in the electrocatalyst. Then, the number of electrons transferred per Ni atom, θ, is calculated by:

$$\theta = \frac{n_e}{n_{Ni}}$$

Then $Ni(OH)_2$ shows 1.6 e./Ni atom and $Ni(OH)_2$@FeOOH show 0.03 e./Ni atom (based on reduction peak).

In-situ X-ray Absorption Spectroscopy (XAS) Characterization

In-situ XAS setup and Characterization

The XAS measurements were conducted in fluorescence mode with a four-element Vortex detector at the PIPOXS beamline of the Cornell High Energy Synchrotron Source (CHESS) under ring conditions of 100 mA and 6 GeV. The incident beam was energy selected using a liquid nitrogen cooled Si(111) monochromator, and the beam was 1×2 mm at the sample, and harmonic rejection was achieved using a pair of Rh-coated mirrors. Ni K edge spectra were collected from 8.2 to 9.0 keV and were calibrated using the Ni foil absorption K edge at 8333.0 eV (determined from the maximum of the first derivative). Fe K edge spectra were collected from 7.05 to 7.75 keV and were calibrated using the Fe foil absorption K edge at 7112.0 eV (determined from the maximum of the first derivative). In-situ electrochemical XAS measurements were conducted using a custom-designed PEEK (polyether ether ketone) electrochemical cell, as described previously. [59]

The electrocatalysts were applied onto a 1 × 1 cm^2 area of a carbon cloth strip (approximately 200 μm thick) using the customized ultrasonic spray system to achieve a loading of 0.5 mg/cm^2 to maximize signal intensity while also limiting self-absorption, and this region loaded with the catalyst was positioned facing the electrolyte in the in-situ X-ray electrochemical cell. A carbon rod was used as the CE, and an RHE RE was connected to the cell using a Luggin capillary. The cell was filled with Fe-free 1 M KOH and purged with Ar during the experiments. XAS spectra were acquired at different potentials, ranging from 1.2 to 1.8 V (vs. RHE) with 0.2 V intervals. Spectra were averaged from 3 scans to improve the signal-to-noise ratio to reach a minimum k value of 11 in FT-EXAFS data. A new spot was used after every 3 scans to ensure no beam damage.

.

Determination of bond information and chemical valence of Ni and Fe

Fourier transformation of the EXAFS spectra was conducted using the Athena and Artemis software packages [60] With a Hanning window from 3 to 11 $Å^{-1}$ with k^2 weighting and without phase correction. The valence states of the metal centers at different applied potentials were determined by correlating the XANES edge energy with the oxidation state, using reference compounds with similar coordination environments and known valence states. Both nickel(oxy)hydroxide reference samples (Fig. S31) including NiO, α-$Ni(OH)_2$, β-$Ni(OH)_2$, and NiOOH. Fe (oxy)hydroxide reference samples (Fig. S32) including FeO, Fe_3O_4, Fe_2O_3, α-FeOOH, β-FeOOH, and γ-FeOOH shows a linear relationship between oxidation state and edge energy, similar to previous report [61]. The valence states of Ni and Fe centers at different potentials were then extrapolated from the fitted curve.

Electron Microscopy Methodology

Electron Microscope

The Electron microscope data are collected with Kraken (Thermo-Fisher FEI Spectra 300 TEM with ultra-high-brightness cold field emission gun (C-FEG) and probe spherical aberration

correction). All the data are taken with a 300 kV accelerating voltage at room temperature (300 K) or cryogenic liquid nitrogen temperature (100 K).

TEM sample preparation

Preparation of catalyst powder solution: Standard powder sample preparation for TEM study is applied: 5 mg of powder sample is dispersed in 5 mL 25% ethanol in a 10 mL glass vial and sonicate for 10 minutes in cold bath till a homogenous grey solution is formed and no precipitate can be observed at the bottom of the glass vial. The dispersion of three samples is very good at this concentration, the suspension can hold for a few hours at room temperature without obvious precipitation.

Preparation of TEM grid: 10 μL of the solution above is dipped on a HexAuFoil grid [52,62] and dried in the air naturally. Thus, the loading is 10 μg on the HexAuFoil grid (3.05 mm diameter), leading to 34.2 $\mu g/cm^2$. The geometric density of powder on the TEM grid can be checked with scanning electron microscope (SEM, Figure). The TEM grids are stored in the atmosphere.

HAADF/iDPC imaging

High-angle annular dark-field (HAADF) STEM imaging was performed on the *Kraken* microscope using a 50 μm C2 aperture, a camera length of 115 mm (corresponding to a 60 mrad inner and 200 mrad outer collection angle), a convergence angle of 21.4 mrad, and a beam current of 4 pA. Integral differential phase contrast (iDPC) STEM images were simultaneously acquired using a four-segment ring detector. iDPC and bright-field (BF) image stacks were collected in series with the HAADF images. To improve signal-to-noise ratio and minimize sample drift, the image stacks were summed into a single frame after two-pass rigid registration. [63]

$Ni(OH)_2$ is sensitive to electron beam damage, likely due to the presence of the OH bond, which is easy to be ionized by electrons. Therefore, the total electron dose for $Ni(OH)_2$ was kept below 2000 $e^-/Å^2$. NiOOH and $NiFe(OH)_2$ are more beam-sensitive than $Ni(OH)_2$, owing to both OH bonds and intercalated water/ions. For NiOOH and $NiFe(OH)_2$, the total electron dose was limited to below 400 $e^-/Å^2$ at room temperature and 1000 $e^-/Å^2$ at cryogenic temperature. [64–66]

EELS mapping

The Electron Energy Loss Spectroscopy (EELS) data for elemental mapping was collected on the Kraken with the energy resolution of 0.75 eV with a 0.3 eV/channel and a 90-pA probe current. For elemental mapping, $L_{2,3}$ edge of Fe and $L_{2,3}$ edge of Ni were integrated after linear combination of power-laws with local background averaging background subtraction with Cornell Spectrum Imager. [67]

Cryo-STEM set up and imaging.

To prepare the sample, 10 μL of the catalyst solution was drop-cast onto a HexAuFoil grid and air-dried, resulting in a loading of ~10 μg per 3.05 mm grid (equivalent to 34.2 $\mu g/cm^2$). The HexAuFoil grid was then clipped using an Au reverse tweezer to serve as the working electrode.

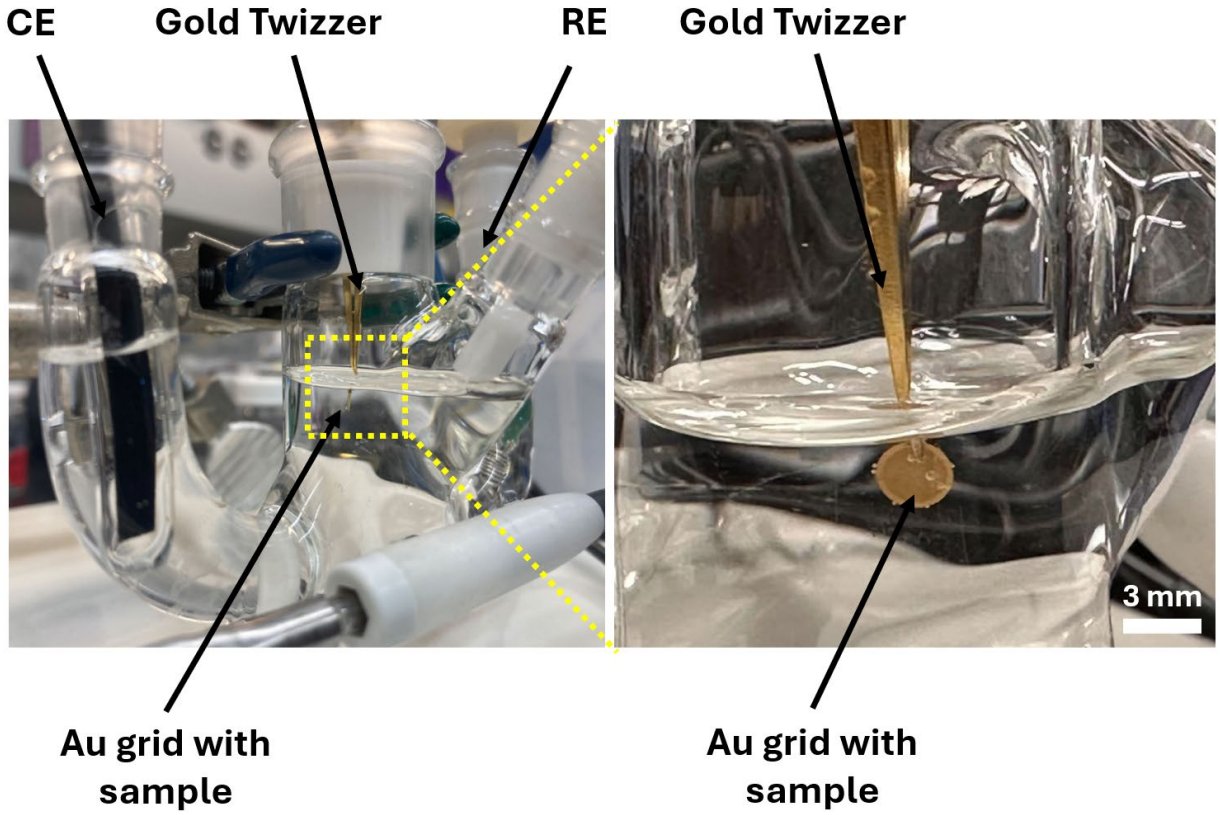
Electrochemical treatment followed the standard RDE setup: chronoamperometry at 1.8 V vs RHE was applied for 100 minutes to fully oxidize the catalyst to its active phase.

After the potential was removed, the grid was gently rinsed with DI water to remove residual 1 M KOH. Excess water was carefully wiped off with a Kimwipe while keeping the grid wet. This post-electrolysis quenching process took approximately 30 seconds.

The wet grid was plunge-frozen using melting solid nitrogen and transferred under liquid nitrogen protection to a cryo holder. The sample was kept at ~100 K throughout transfer and imaging to preserve the active phase.

Cryo-STEM imaging was performed on *Kraken* using a Gatan cryotransfer double-tilt holder at 100 K. At this temperature, the allowable total electron dose is 2-3 times higher than that at room temperature.

Cryo-SEND data were acquired using an electron microscope pixel array detector (EMPAD) [68], with a 256×256 pixel scan in real space. At each pixel, a 128×128 pixel diffraction pattern was collected in reciprocal space with a dwell time of 1 ms, resulting in a full scan time of approximately 1 minute.



Extended Data Fig. 1. Set up of electrochemical reaction before Cryo-STEM
The electrocatalyst is loaded onto a HexAuFoil grid and clipped to an Au tweezer as the working electrode in a regular three-electrode electrochemical testing setup.

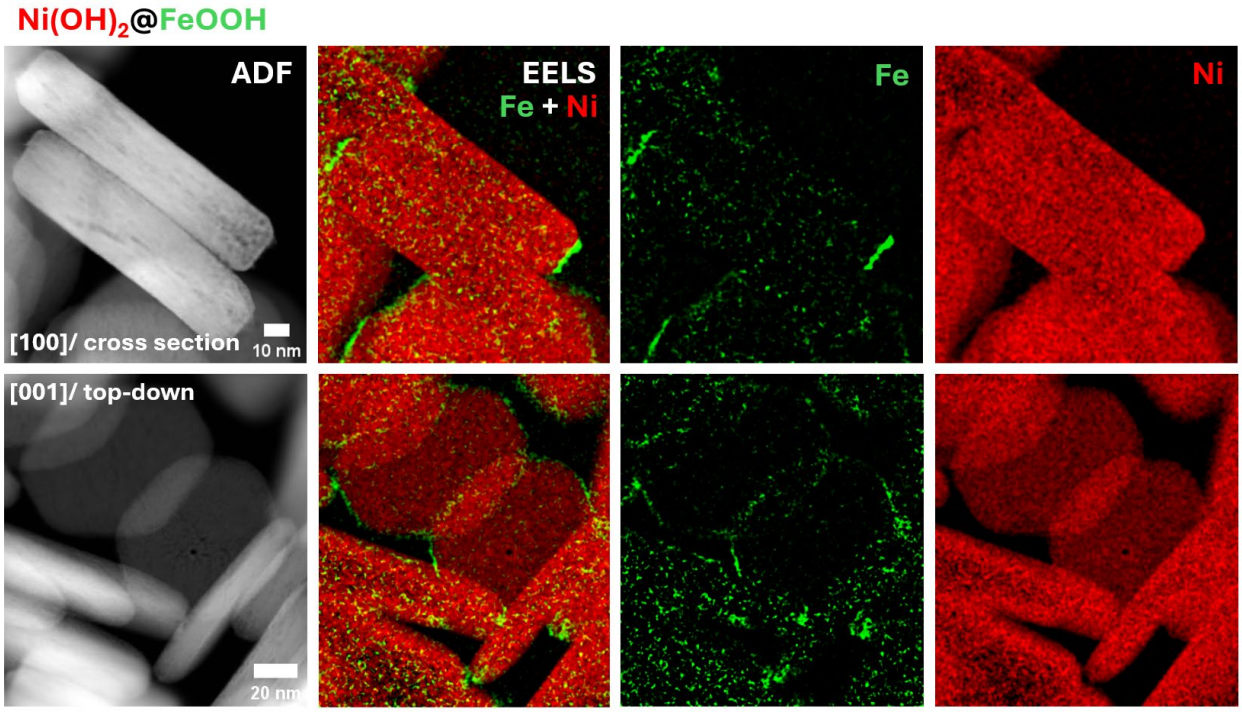
Other Structural Characterization

X-ray Diffraction (XRD)

The PXRD patterns were obtained using a Bruker D8 Advance ECO powder diffractometer equipped with a Cu Kα radiation source (λ = 1.5406 Å). The instrument operated at 1 kW (40 kV and 25 mA), with a step size of 0.01945 degrees and an acquisition time of 0.5 seconds per data point.

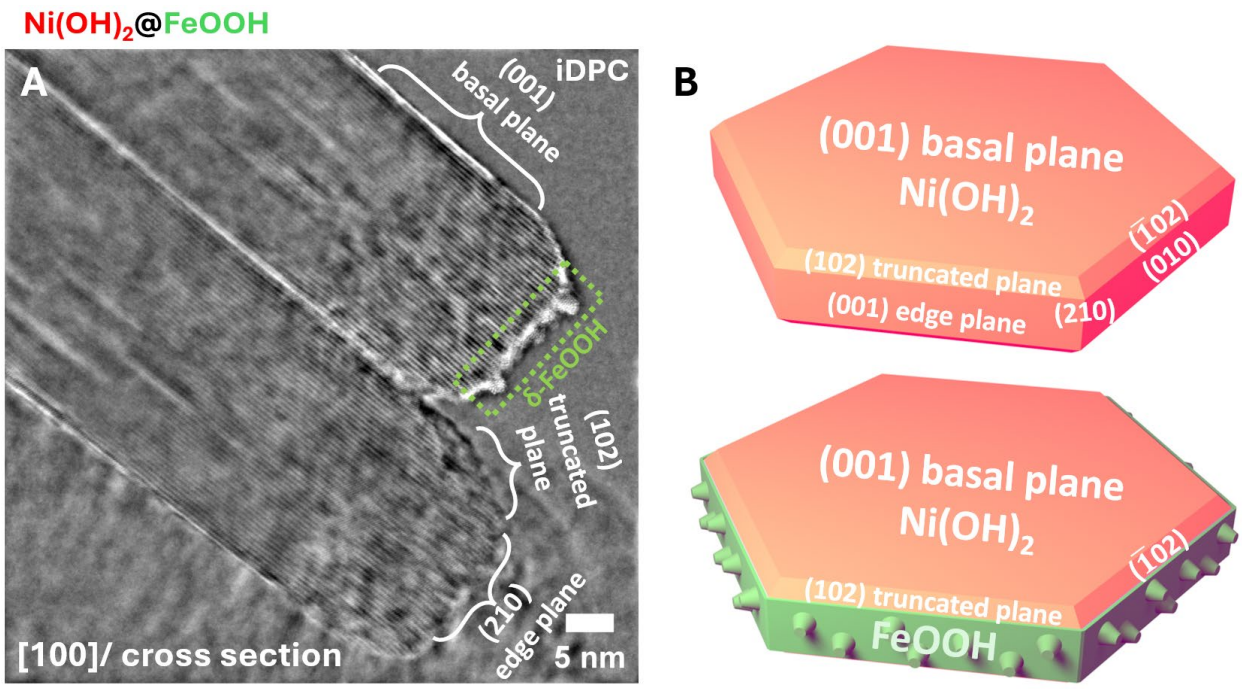
Scanning Electron Microscope (SEM)

The scanning electron microscope (SEM) measurements are carried out on a Zeiss Gemini 500 at 5 kV using an in-lens scattered electron detector.



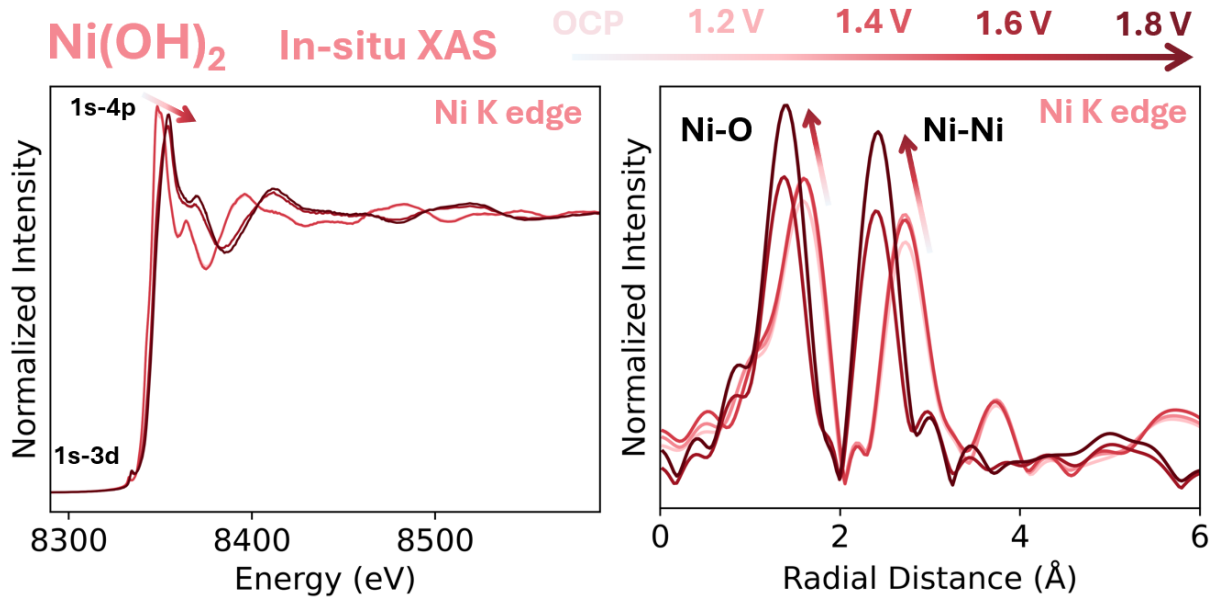
Extended Data Fig. 2. STEM EELS of $Ni(OH)_2$@FeOOH

STEM EELS mapping of Ni and Fe and simultaneous ADF in $Ni(OH)_2$@FeOOH along both [100] side and [001] top-down view, showing that the Fe only selectively grows on the edge plane of $Ni(OH)_2$.

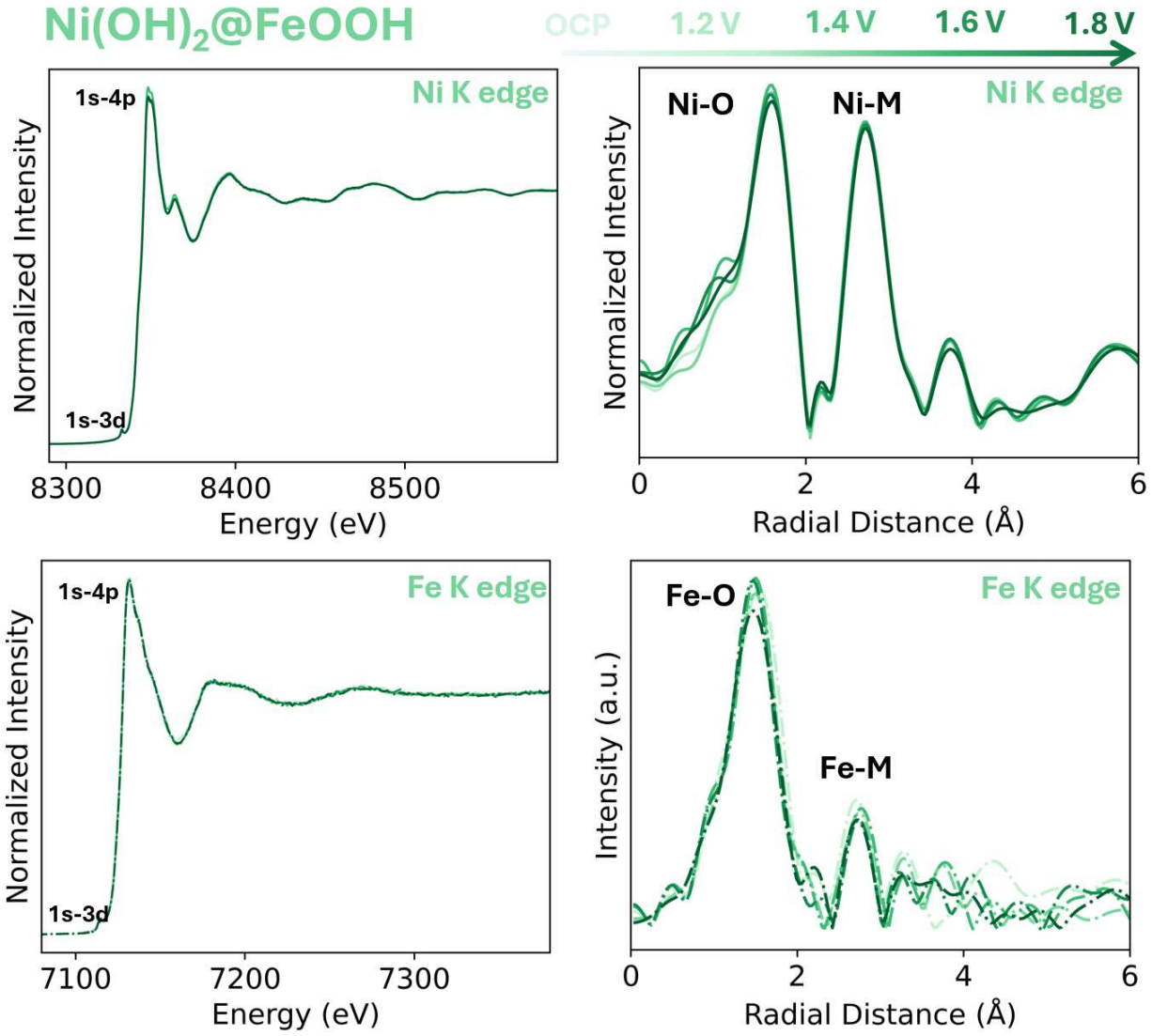


Extended Data Fig. 3. STEM iDPC image of $Ni(OH)_2$@FeOOH and the exposed facets of $Ni(OH)_2$ and $Ni(OH)_2$@FeOOH

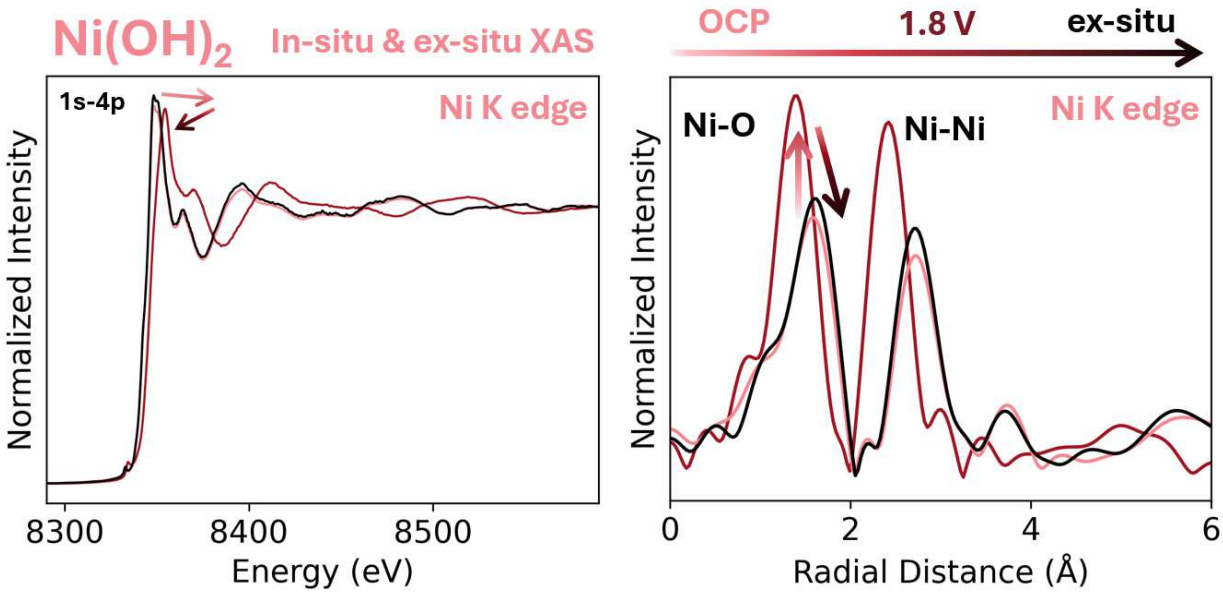
(A) STEM iDPC image of $Ni(OH)_2$@FeOOH showing that the δ-FeOOH selectively grows the edge plane of $Ni(OH)_2$. (B) The schematic figure shows the (001) basal plane, (102) plane truncated plane and (001) edge plane of $Ni(OH)_2$ nanoplates. Combining with the STEM EELS elemental mapping, the δ-FeOOH nanoislands selectively grow on the edge plane of $Ni(OH)_2$ nanoplates.



Extended Data Fig. 4. electrochemical in-situ XANES and FT-EXAFS of $Ni(OH)_2$
Electrochemical in-situ EXAFS and its FFT of $Ni(OH)_2$ from open circuit potential (OCP) to 1.8V vs. RHE, the right energy shift of 1s-4p Ni K edge is obvious in XANES as the potential goes higher. In the k^2-weighted Fourier-transformed EXAFS spectra (without phase correction), the Ni-Ni and Ni-O peaks exhibit a negative shift, indicating the shortening of Ni-Ni and Ni-O bonds from the β-$Ni(OH)_2$ phase to the γ-NiOOH phase at high OER potentials.

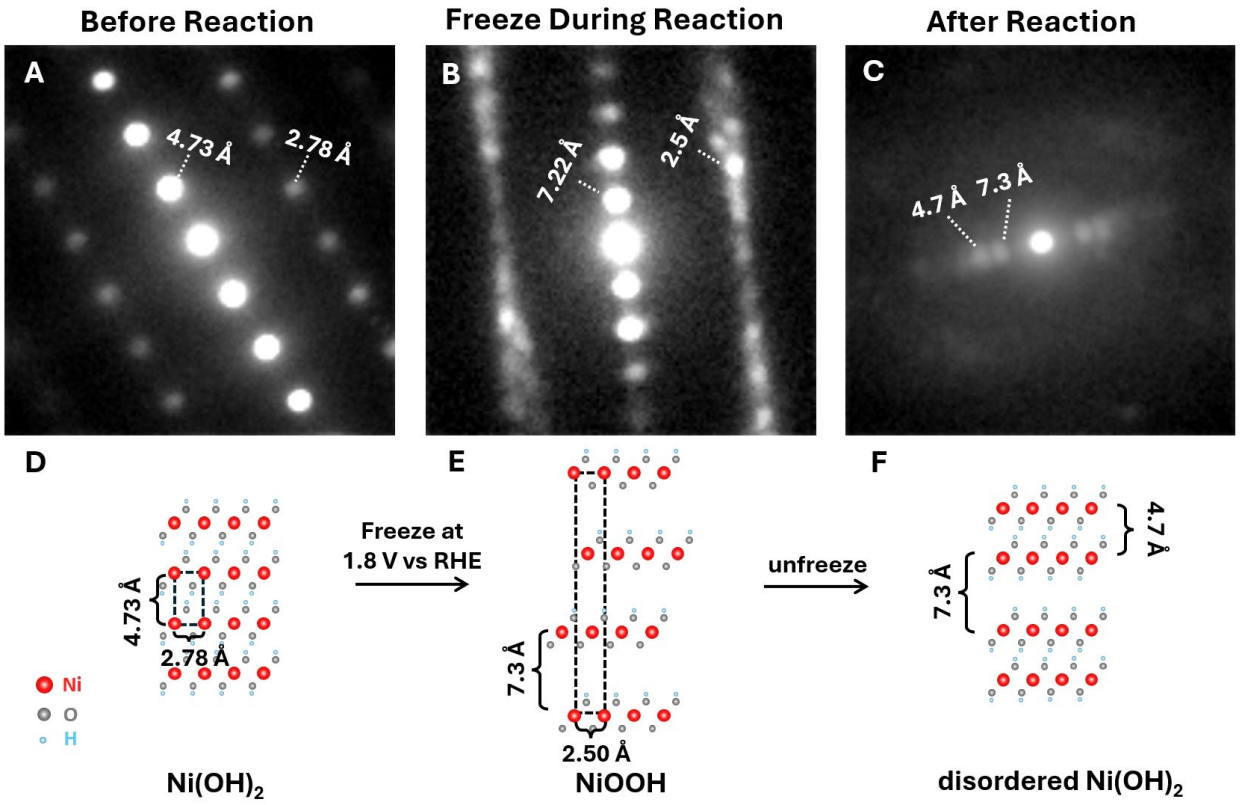


Extended Data Fig. 5. electrochemical in-situ XANES and FT-EXAFS of $Ni(OH)_2$@FeOOH Electrochemical in-situ EXAFS and its FFT of $Ni(OH)_2$@FeOOH from open circuit potential (OCP) to 1.8V vs. RHE, no obvious change in 1s-4p Ni K edge is observed in XANES as the potential goes higher. In the k^2-weighted Fourier-transformed EXAFS spectra (without phase correction), the Ni-O and Ni-M peaks show no obvious shift in radial distance, meaning the majority of β-$Ni(OH)_2$ phase is retained at high OER potentials. The Fe exists as δ-FeOOH on the $Ni(OH)_2$ edge plane, and its XANES and the k^2-weighted Fourier-transformed EXAFS spectra (without phase correction) have a different shape from those of Ni, indicating that Fe exists in a different phase. No obvious changes in Fe-O and Fe-M peaks are observed under OER conditions.



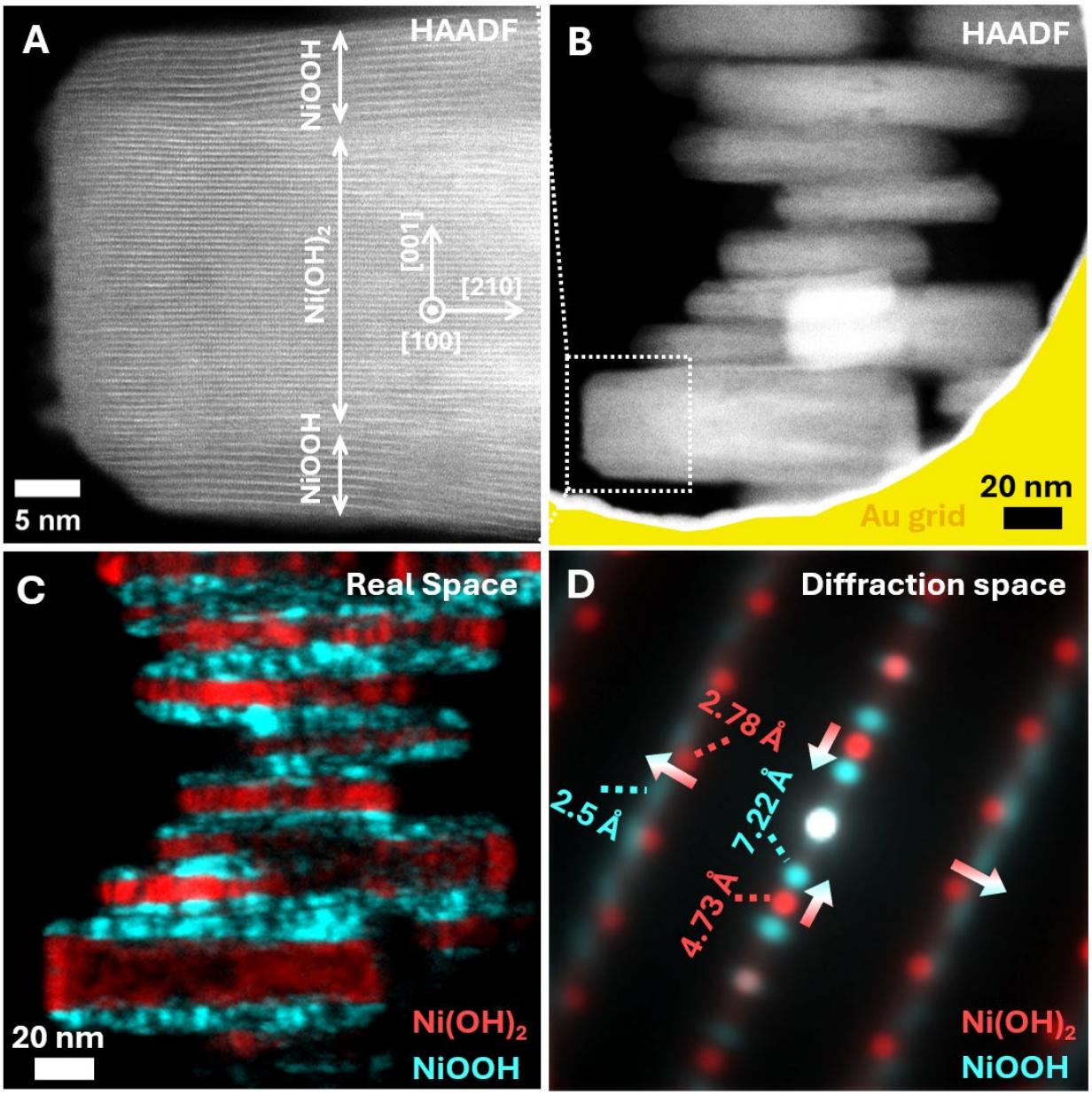
Extended Data Fig. 6. in-situ and ex-situ XANES and FT-EXAFS of $Ni(OH)_2$, showing that the NiOOH returns to $Ni(OH)_2$ after removing the potential

Comparison between in-situ and ex-situ XANES and the k^2-weighted Fourier-transformed EXAFS spectra (without phase correction) of $Ni(OH)_2$, shows that the $Ni(OH)_2$ transform to γ-NiOOH phase at 1.8V vs RHE, and goes back to $Ni(OH)_2$ ex-situ (resting the sample in room temperature overnight). These results represent the unstable nature of active phase of electrocatalysts at working potentials



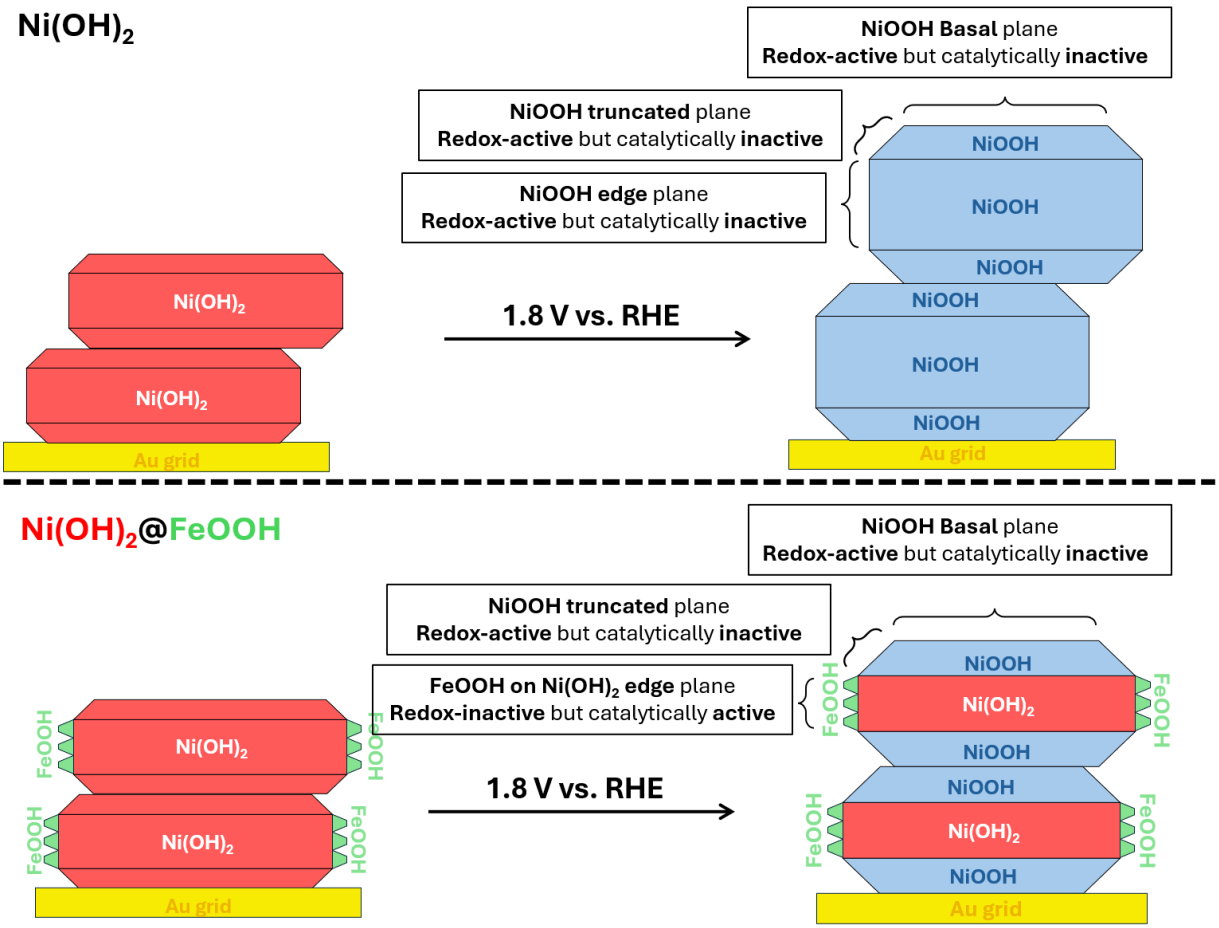
Extended Data Fig. 7. SEND of $Ni(OH)_2$, Cryo-SEND of NiOOH, and SEND of ex-situ disordered $Ni(OH)_2$

Scanning electron nanobeam diffraction (SEND) of initial $Ni(OH)_2$, Cryo-SEND of NiOOH, and SEND of ex-situ disordered $Ni(OH)_2$. The initial $Ni(OH)_2$ has a very ordered diffraction pattern with 4.73 Å interlayer displacing and 2.78 Å in-plane Ni-Ni displacing. The NiOOH, oxidized from $Ni(OH)_2$ at 1.8 V vs RHE, has a larger 7.22 Å interlayer displacing and a shorter 2.50 Å in-plane Ni-Ni displacing from Cryo-SEND. From the Cryo-SEND of NiOOH, its crystal structure is also a bit disordered. The ex-situ SEND measurement of NiOOH shows that it decays to a disordered $Ni(OH)_2$ with both 4.7 Å and 7.2 Å interlayer displacing. No obvious in-plane displacing can be found, indicating that the structure of ex-situ $Ni(OH)_2$ is very disordered, matching its STEM HAADF image



Extended Data Fig. 8. Cryo-STEM HAADF and Cryo-SEND image of metastable structure of $Ni(OH)_2$@FeOOH

(A) Atomic resolution Cryo-STEM HAADF image of $Ni(OH)_2$@FeOOH from side view shows the outmost top and bottom $Ni(OH)_2$ layers are oxidized to NiOOH in $Ni(OH)_2$@FeOOH. (B) A zoom-out larger field-of-view Cryo-STEM HAADF image and (C-D) Cryo-SEND data confirm that this structural transformation is consistent across multiple nanoplates. Similar to elemental mapping, but for crystal structure rather than chemical composition, Cryo-SEND visualizes different phases: in our case, cyan corresponds to NiOOH and red to $Ni(OH)_2$. In each nanoplate, red is concentrated in the core, while cyan appears only at the top and bottom layers, indicating that oxidation is confined to the outermost and uncovered $Ni(OH)_2$ layers. NiOOH is observed only at the outermost layers, forming a vertical (NiOOH@$Ni(OH)_2$@NiOOH) heterostructure within a lateral heterostructure ($Ni(OH)_2$@FeOOH).



Extended Data Fig. 9. Comparing the structural change of $Ni(OH)_2$ and $Ni(OH)_2$@FeOOH during OER

This schematic figure, based on both atom-resolution and large field-of-view Cryo-STEM images, summarizes the structural transformation of $Ni(OH)_2$ and $Ni(OH)_2$@FeOOH during the OER reaction. It also distinguishes redox-active from catalytically active sites in the metastable structure of $Ni(OH)_2$@FeOOH during OER. We define redox-active sites as metal centers that undergo oxidation or reduction under applied potential, whereas catalytically active sites are those that drive the OER. In the case of pure $Ni(OH)_2$, which fully oxidizes to NiOOH under OER conditions, all surface planes—basal, truncated, and edge—are redox-active. However, none of these surfaces exhibit significant catalytic activity relative to $Ni(OH)_2$@FeOOH. While it is often believed that the edge plane of NiOOH may be more catalytically active than basal planes, all planes in the NiOOH structure remain relatively catalytically inactive overall. Notably, $Ni(OH)_2$@FeOOH shares similar basal and truncated surface structures with NiOOH, but only the edge-linked FeOOH distinguishes it structurally. Since these FeOOH-covered edge planes are the unique surface feature and correlate with the enhanced activity, we attribute the catalytically active sites to the Fe^{3+} centers in FeOOH on the $Ni(OH)_2$ edge planes. These sites are redox-inactive yet catalytically active, highlighting that redox activity is not a prerequisite for catalytic activity.

Reference

1. Lopes, P. P. *et al.* Dynamically Stable Active Sites from Surface Evolution of Perovskite Materials during the Oxygen Evolution Reaction. *J. Am. Chem. Soc.* **143**, 2741–2750 (2021).
2. Vogt, C. & Weckhuysen, B. M. The concept of active site in heterogeneous catalysis. *Nat Rev Chem* **6**, 89–111 (2022).
3. Ning, M. *et al.* Dynamic Active Sites in Electrocatalysis. *Angewandte Chemie* **136**, e202415794 (2024).
4. Friebel, D. *et al.* Identification of Highly Active Fe Sites in (Ni,Fe)OOH for Electrocatalytic Water Splitting. *J. Am. Chem. Soc.* **137**, 1305–1313 (2015).
5. Chen, J. Y. C. *et al.* Operando Analysis of NiFe and Fe Oxyhydroxide Electrocatalysts for Water Oxidation: Detection of Fe4+ by Mössbauer Spectroscopy. *J. Am. Chem. Soc.* **137**, 15090–15093 (2015).
6. Görlin, M. *et al.* Tracking Catalyst Redox States and Reaction Dynamics in Ni–Fe Oxyhydroxide Oxygen Evolution Reaction Electrocatalysts: The Role of Catalyst Support and Electrolyte pH. *J. Am. Chem. Soc.* **139**, 2070–2082 (2017).
7. Li, A. *et al.* Atomically dispersed hexavalent iridium oxide from MnO2 reduction for oxygen evolution catalysis. *Science* **384**, 666–670 (2024).
8. Maiyalagan, T., Jarvis, K. A., Therese, S., Ferreira, P. J. & Manthiram, A. Spinel-type lithium cobalt oxide as a bifunctional electrocatalyst for the oxygen evolution and oxygen reduction reactions. *Nat Commun* **5**, 3949 (2014).
9. Deka, N. *et al.* On the Operando Structure of Ruthenium Oxides during the Oxygen Evolution Reaction in Acidic Media. *ACS Catal.* **13**, 7488–7498 (2023).

10. Li, L. *et al.* In Situ/Operando Capturing Unusual Ir6+ Facilitating Ultrafast Electrocatalytic Water Oxidation. *Advanced Functional Materials* **31**, 2104746 (2021).
11. Wang, H. *et al.* High-Valence Oxides for High Performance Oxygen Evolution Electrocatalysis. *Advanced Science* **10**, 2301706 (2023).
12. Li, Y. *et al.* Hexavalent Ru Catalyst with Both Lattice Oxygen and Metal Ion Mechanisms Coactive for Water Oxidation. *J. Am. Chem. Soc.* **147**, 26854–26864 (2025).
13. Zhao, Y. *et al.* Oxygen Evolution/Reduction Reaction Catalysts: From In Situ Monitoring and Reaction Mechanisms to Rational Design. *Chem. Rev.* **123**, 6257–6358 (2023).
14. Ertl, G. Basic Principles. in *Reactions at Solid Surfaces* 1–19 (John Wiley & Sons, Ltd, 2009). doi:10.1002/9780470535295.ch1.
15. Fabbri, E. *et al.* Dynamic surface self-reconstruction is the key of highly active perovskite nano-electrocatalysts for water splitting. *Nature Mater* **16**, 925–931 (2017).
16. Chung, D. Y. *et al.* Dynamic stability of active sites in hydr(oxy)oxides for the oxygen evolution reaction. *Nat Energy* **5**, 222–230 (2020).
17. May, K. J. *et al.* Influence of Oxygen Evolution during Water Oxidation on the Surface of Perovskite Oxide Catalysts. *J. Phys. Chem. Lett.* **3**, 3264–3270 (2012).
18. Desilvestro, J., Corrigan, D. A. & Weaver, M. J. Characterization of Redox States of Nickel Hydroxide Film Electrodes by In Situ Surface Raman Spectroscopy. *J. Electrochem. Soc.* **135**, 885 (1988).
19. Shih, A. J. *et al.* Water electrolysis. *Nat Rev Methods Primers* **2**, 1–19 (2022).
20. Grigoriev, S. A., Fateev, V. N., Bessarabov, D. G. & Millet, P. Current status, research trends, and challenges in water electrolysis science and technology. *International Journal of Hydrogen Energy* **45**, 26036–26058 (2020).

21. Zhu, K., Zhu, X. & Yang, W. Application of In Situ Techniques for the Characterization of NiFe-Based Oxygen Evolution Reaction (OER) Electrocatalysts. *Angewandte Chemie International Edition* **58**, 1252–1265 (2019).
22. Magnier, L. *et al.* Fe–Ni-based alloys as highly active and low-cost oxygen evolution reaction catalyst in alkaline media. *Nat. Mater.* **23**, 252–261 (2024).
23. Dionigi, F. & Strasser, P. NiFe-Based (Oxy)hydroxide Catalysts for Oxygen Evolution Reaction in Non-Acidic Electrolytes. *Advanced Energy Materials* **6**, 1600621 (2016).
24. Anantharaj, S., Kundu, S. & Noda, S. "The Fe Effect": A review unveiling the critical roles of Fe in enhancing OER activity of Ni and Co based catalysts. *Nano Energy* **80**, 105514 (2021).
25. Roldán Cuenya, B. & Bañares, M. A. Introduction: Operando and In Situ Studies in Catalysis and Electrocatalysis. *Chem. Rev.* **124**, 8011–8013 (2024).
26. Magnussen, O. M. *et al.* In Situ and Operando X-ray Scattering Methods in Electrochemistry and Electrocatalysis. *Chem. Rev.* **124**, 629–721 (2024).
27. Deng, J. *et al.* Morphology Dynamics of Single-Layered Ni(OH)2/NiOOH Nanosheets and Subsequent Fe Incorporation Studied by in Situ Electrochemical Atomic Force Microscopy. *Nano Lett.* **17**, 6922–6926 (2017).
28. Trześniewski, B. J. *et al.* In Situ Observation of Active Oxygen Species in Fe-Containing Ni-Based Oxygen Evolution Catalysts: The Effect of pH on Electrochemical Activity. *J. Am. Chem. Soc.* **137**, 15112–15121 (2015).
29. Mefford, J. T. *et al.* Correlative operando microscopy of oxygen evolution electrocatalysts. *Nature* **593**, 67–73 (2021).

30. Wu, Z.-P. *et al.* Potential Pulsing-Induced Fe Undercoordination in NiFe (Oxy)Hydroxide Enhances Electrochemical Oxygen Evolution. *J. Am. Chem. Soc.* **147**, 36763–36773 (2025).
31. Dionigi, F. *et al.* In-situ structure and catalytic mechanism of NiFe and CoFe layered double hydroxides during oxygen evolution. *Nat Commun* **11**, 2522 (2020).
32. Oliva, P. *et al.* Review of the structure and the electrochemistry of nickel hydroxides and oxy-hydroxides. *Journal of Power Sources* **8**, 229–255 (1982).
33. Trotochaud, L., Young, S. L., Ranney, J. K. & Boettcher, S. W. Nickel–Iron Oxyhydroxide Oxygen-Evolution Electrocatalysts: The Role of Intentional and Incidental Iron Incorporation. *J. Am. Chem. Soc.* **136**, 6744–6753 (2014).
34. Guo, B. *et al.* Iron Oxyhydroxide: Structure and Applications in Electrocatalytic Oxygen Evolution Reaction. *Advanced Functional Materials* **33**, 2300557 (2023).
35. Zhukhlistov, A. P. Crystal structure of lepidocrocite FeO(OH) from the electron-diffractometry data. *Crystallogr. Rep.* **46**, 730–733 (2001).
36. Görlin, M. *et al.* Oxygen Evolution Reaction Dynamics, Faradaic Charge Efficiency, and the Active Metal Redox States of Ni–Fe Oxide Water Splitting Electrocatalysts. *J. Am. Chem. Soc.* **138**, 5603–5614 (2016).
37. Klingenhof, M. *et al.* High-performance anion-exchange membrane water electrolysers using NiX (X = Fe,Co,Mn) catalyst-coated membranes with redox-active Ni–O ligands. *Nat Catal* **7**, 1213–1222 (2024).
38. Shen, H. *et al.* Durable Anion Exchange Membrane Water Electrolysis in Low-Alkaline Concentration Electrolyte. *J. Am. Chem. Soc.* **147**, 22677–22685 (2025).

39. Seijas-Da Silva, A. *et al.* Scalable synthesis of NiFe-layered double hydroxide for efficient anion exchange membrane electrolysis. *Nat Commun* **16**, 6138 (2025).
40. Lu, S.-Y. *et al.* Synthetic tuning stabilizes a high-valence Ru single site for efficient electrolysis. *Nat. Synth* **3**, 576–585 (2024).
41. Stevens, M. B., Trang, C. D. M., Enman, L. J., Deng, J. & Boettcher, S. W. Reactive Fe-Sites in Ni/Fe (Oxy)hydroxide Are Responsible for Exceptional Oxygen Electrocatalysis Activity. *J. Am. Chem. Soc.* **139**, 11361–11364 (2017).
42. Ou, Y. *et al.* Cooperative Fe sites on transition metal (oxy)hydroxides drive high oxygen evolution activity in base. *Nat Commun* **14**, 7688 (2023).
43. Corrigan, D. A. & Knight, S. L. Electrochemical and Spectroscopic Evidence on the Participation of Quadrivalent Nickel in the Nickel Hydroxide Redox Reaction. *J. Electrochem. Soc.* **136**, 613 (1989).
44. Capehart, T. W., Corrigan, D. A., Conell, R. S., Pandya, K. I. & Hoffman, R. W. In situ extended x-ray absorption fine structure spectroscopy of thin-film nickel hydroxide electrodes. *Applied Physics Letters* **58**, 865–867 (1991).
45. Balasubramanian, M., Melendres, C. A. & Mini, S. X-ray Absorption Spectroscopy Studies of the Local Atomic and Electronic Structure of Iron Incorporated into Electrodeposited Hydrous Nickel Oxide Films. *J. Phys. Chem. B* **104**, 4300–4306 (2000).
46. Ali-Löytty, H. *et al.* Ambient-Pressure XPS Study of a Ni–Fe Electrocatalyst for the Oxygen Evolution Reaction. *J. Phys. Chem. C* **120**, 2247–2253 (2016).
47. Goldsmith, Z. K. *et al.* Characterization of NiFe oxyhydroxide electrocatalysts by integrated electronic structure calculations and spectroelectrochemistry. *Proceedings of the National Academy of Sciences* **114**, 3050–3055 (2017).

48. Zachman, M. J., Tu, Z., Choudhury, S., Archer, L. A. & Kourkoutis, L. F. Cryo-STEM mapping of solid–liquid interfaces and dendrites in lithium-metal batteries. *Nature* **560**, 345–349 (2018).
49. Panova, O. *et al.* Diffraction imaging of nanocrystalline structures in organic semiconductor molecular thin films. *Nat. Mater.* **18**, 860–865 (2019).
50. Li, Y. *et al.* Electrified Operando-Freezing of Electrocatalytic CO2 Reduction Cells for Cryogenic Electron Microscopy. *Nano Lett.* **24**, 10409–10417 (2024).
51. Yao, N., Lamb, K., Yan, N. & Han, Y. Voltage-Gating Device (VGD) for Cryogenic Electron Microscopy (Cryo-EM). https://collaborate.princeton.edu/en/publications/voltage-gating-device-vgd-for-cryogenic-electron-microscopy-cryo- (2019).
52. Naylor, C., Thaw, P. & Vandekerckhove, H. Achieving high-throughput, high-quality imaging for SPA with HexAuFoil® sample supports. *Structural Dynamics* **12**, A60 (2025).
53. Zuo, J.-M. & Tao, J. Scanning Electron Nanodiffraction and Diffraction Imaging. in *Scanning Transmission Electron Microscopy: Imaging and Analysis* (eds Pennycook, S. J. & Nellist, P. D.) 393–427 (Springer, New York, NY, 2011). doi:10.1007/978-1-4419-7200-2_9.
54. Sac-Epée, N., Palacìn, M. R., Delahaye-Vidal, A., Chabre, Y. & Tara⁄scon, J.-M. Evidence for Direct γ - NiOOH ↔ β - Ni (OH) 2 Transitions during Electrochemical Cycling of the Nickel Hydroxide Electrode. *J. Electrochem. Soc.* **145**, 1434 (1998).
55. Dong, L., Chu, Y. & Sun, W. Controllable Synthesis of Nickel Hydroxide and Porous Nickel Oxide Nanostructures with Different Morphologies. *Chemistry – A European Journal* **14**, 5064–5072 (2008).

56. Jaśkaniec, S. *et al.* Low-temperature synthesis and investigation into the formation mechanism of high quality Ni-Fe layered double hydroxides hexagonal platelets. *Sci Rep* **8**, 4179 (2018).
57. Trotochaud, L., Young, S. L., Ranney, J. K. & Boettcher, S. W. Nickel–Iron Oxyhydroxide Oxygen-Evolution Electrocatalysts: The Role of Intentional and Incidental Iron Incorporation. *J. Am. Chem. Soc.* **136**, 6744–6753 (2014).
58. Mefford, J. T., Akbashev, A. R., Zhang, L. & Chueh, W. C. Electrochemical Reactivity of Faceted β-Co(OH)2 Single Crystal Platelet Particles in Alkaline Electrolytes. *J. Phys. Chem. C* **123**, 18783–18794 (2019).
59. Li, Q. *et al.* Operando X-ray absorption spectroscopic investigation of electrocatalysts state in anion exchange membrane fuel cells. *Nat Commun* **16**, 3008 (2025).
60. Ravel, B. & Newville, M. ATHENA, ARTEMIS, HEPHAESTUS: data analysis for X-ray absorption spectroscopy using IFEFFIT. *J Synchrotron Rad* **12**, 537–541 (2005).
61. Li, Q. *et al.* Operando X-ray absorption spectroscopic investigation of electrocatalysts state in anion exchange membrane fuel cells. *Nat Commun* **16**, 3008 (2025).
62. Naydenova, K., Jia, P. & Russo, C. J. Cryo-EM with sub–1 Å specimen movement. *Science* **370**, 223–226 (2020).
63. Savitzky, B. H. *et al.* Image registration of low signal-to-noise cryo-STEM data. *Ultramicroscopy* **191**, 56–65 (2018).
64. Carpenter, G. J. & Wronski, Z. S. De-protonation of Nickel Hydroxide by 200 kV Electron Irradiation. *Microscopy Today* **29**, 26–29 (2021).

65. Hobbs, C., Downing, C., Jaskaniec, S. & Nicolosi, V. TEM and EELS characterization of Ni–Fe layered double hydroxide decompositions caused by electron beam irradiation. *npj 2D Mater Appl* **5**, 1–9 (2021).
66. Shi, Z., Li, Q., Abruña, H. D. & Muller, D. A. Identifying the Active Sites of NiFe Hydroxides by Low-Dose Electron Microscopy and In Situ X-ray Absorption Spectroscopy. *Microscopy and Microanalysis* **30**, ozae044.1046 (2024).
67. Cueva, P., Hovden, R., Mundy, J. A., Xin, H. L. & Muller, D. A. Data Processing for Atomic Resolution Electron Energy Loss Spectroscopy. *Microscopy and Microanalysis* **18**, 667–675 (2012).
68. Tate, M. W. *et al.* High Dynamic Range Pixel Array Detector for Scanning Transmission Electron Microscopy. *Microscopy and Microanalysis* **22**, 237–249 (2016).

Acknowledgments: ZX Shi thanks Dr. Cara Gannett for her advice for synthesis, Dr. Hongbin Yang for his suggestions on SEND, Logan Smith and Dr. Kai Cui from Prof. Sharon Hammes-Schiffer group for discussion on PCET, John Grazul for maintaining the "Kraken" electron microscope.

Funding:

Center for Alkaline Based Energy Solutions (CABES), an Energy Frontier Research Center funded by the U. S. Department of Energy (DOE), Office of Science, Basic Energy Sciences at Cornell University under award # DE-SC0019445

US National Science Foundation grant DMR-1719875 (Cornell Center for Materials Research shared instrumentation)

US National Science Foundation grant DMR-2039380, the Weill Institute, the Kavli Institute at Cornell, and Cornell University (FEI Spectra 300 transmission electron microscope, aka. "Kraken" at Cornell)

US National Science Foundation (BIO, ENG and MPS Directorates) under award DMR-2342336, the Center for High-Energy X-ray Sciences (CHEXS).

YM. Han acknowledges the Welch Foundation (C-2065 and X-C-0011) and ACS PRF (67236-DNI10) as well as RAMI and SI at Rice University.

Author contributions:

Conceptualization: ZS, HDA, DAM

Methodology: ZS, QL

Investigation: ZS, QL (ZS for TEM, sample preparation, electrochemistry and XAS, QL for electrochemistry and XAS)

Visualization: ZS, QL

Funding acquisition: YH, HDA, DAM

Project administration: ZS, YH, HDA, DAM

Supervision: YH, HDA, DAM

Writing – original draft: ZS, YH, HDA, DAM

Writing – review & editing: all co-authors

Competing interests: Authors declare that they have no competing interests.

Data and materials availability: All data is available in the manuscript or the supplementary materials.

Supplementary Materials

Supplementary Text

Figs. S1 to S27

References (*1–68*)

Supplementary Video

Supplementary Files

This is a list of supplementary files associated with this preprint. Click to download.

- 20260319NiFehydroxideCryoSTEMSINature.pdf
- CatalystonTEMgrid100mAcm2.mp4